Faraday instability and nonlinear pattern formation of a two-layer system: A reduced model

Michael Bestehorn*
Department of Statistical Physics and Nonlinear Dynamics, Brandenburg University of Technology, Platz der Deutschen Einheit 1, 03046 Cottbus, Germany

Andrey Pototsky
Department of Mathematics, Faculty of Science Engineering and Technology, Swinburne University of Technology, Hawthorn, Victoria 3122, Australia
(Received 31 May 2016; published 26 October 2016)

Stability and pattern formation of a two-layer liquid system with large aspect ratio subjected to vertical harmonic oscillations is studied by means of an integrated boundary layer model. The lower layer rests on an oscillating solid substrate, the upper layer is separated by a deformable interface from the lower layer and bounded at the top with a second, free interface to the ambient passive air. The model is derived from the Navier-Stokes equations in long-wave approximation, including inertial terms. Applying a Floquet analysis, linear stability charts and dispersion relations are computed and compared with results from the full linearized Navier-Stokes equations and the long-wave approximation. Nonlinear Faraday patterns simultaneously occurring at the interface and at the film surface are studied by numerically solving the integrated boundary layer model in two and three spatial dimensions. For gravitationally stable two-layer films with a lighter fluid on top of the heavier fluid, we find squares, hexagons, quasiperiodic patterns with eightfold symmetry as well as localized states in the form of large scale depletion regions or finite depth holes, occurring at the interface and surface. For a Rayleigh-Taylor unstable combination (heavier fluid above the light one) we show that external vibration increases the lifetime of the film by delaying or completely suppressing the film rupture.

DOI: 10.1103/PhysRevFluids.1.063905

I. INTRODUCTION

The study of instabilities and subsequent pattern formation in liquids with a free upper surface placed on a vertically vibrating substrate goes back to Faraday in 1831 [1]. In these and in following experiments over the last 185 years, a surface deformation in the form of quite regular patterns, normally squares, is observed which oscillates often with half of the driver's frequency [2]. The wavelength of the structures are thereby in resonance with gravity waves of the unforced liquid. More than 120 years after Faraday, Benjamin and Ursell [3] showed by a linear analysis the instability of an inviscid fluid under vertical vibrations, described by a Mathieu equation. This analysis was extended to viscous fluids [4,5] in thin and thick layers and experimentally confirmed in Ref. [6]. Besides Faraday's subharmonic structures, also harmonic branches where detected later in experiments, for example [7], where the patterns oscillate with the same frequency as the driver. For larger aspect ratios the patterns are regular and may emerge as the classical squares, but also stripes, hexagons [8], or even quasicrystals with 8-fold [9] or 12-fold symmetries [10,11] can be encountered.

Until today, only few papers deal with numerical solutions of the full nonlinear hydrodynamic equations for the standard Faraday instability, almost all of them in one-layer systems and in two dimensions [12–14]. Some recent three-dimensional (3D) work has been performed by the group of Tuckerman [15–17]. An alternate way to tackle the problem numerically is to resort to a reduced description that may apply for thin fluid layers. This method is reported in Refs. [18,19] where an

*Corresponding author: bestehorn@b-tu.de

integrated boundary layer model is derived and the normal direction is integrated out. The system of (2+1)-dimensional governing equations is then closed using a Karman-Pohlhausen approach [20].

The present work is an extension of this model to a two-layer system of immiscible liquids, where both layers fulfill the long-wave (lubrication) condition. The model fully includes inertia in both layers, an important ingredient for parametric instabilities. Due to its simplicity, the model allows us to compute pattern formation also in three dimensions which is desirable since structures emerging from the Faraday instability are essentially three dimensional (squares, hexagons, quasicrystals).

The main purpose of the present paper is to derive and solve numerically the reduced nonlinear model describing the instabilities and pattern formation of a two-layer system. Starting with the Navier-Stokes equations, two consecutive approximation steps are performed. The first one is an extended lubrication or long-wave approximation where the inertial terms of the Navier-Stokes equations have to be retained. The second one consists of integrating out separately for each layer the vertical dependencies of the variables leading to a nonlinear integrated layer model. This model is then solved numerically.

After defining the system, the basic equations in the long-wave approximation, and the boundary and interface condition, we derive in Sec. III the integrated layer model where the number of the spatial dimensions of the original problem is reduced by one by averaging over the vertical direction in each layer. Stability charts for the vibrated as well as dispersion relations for the nondriven system are discussed in Sec. IV for the three cases, (i) full linearized Navier-Stokes equations, (ii) linearized Navier-Stokes equations in the long-wave approximation, (iii) linearized integrated layer model, and compared with each other for several fluid parameter combinations. We extract the data for (i) from our recent paper [21], those for (ii) are computed in the Appendix B. The reader may consider the linear stability section, Sec. IV, as a check for the reliability of the integrated layer model. As long as the structures are long wave, i.e., varying slowly in the horizontal direction, the agreement between long-wave Navier-Stokes equations and the integrated layer model concerning both stability charts and dispersion relations is high. Even for smaller horizontal wavelength the main approximation error comes from the long-wave approximation and not from the integration over the vertical direction.

An important issue is the coupling of the two interfaces of the system: The deformations of the film surface and the liquid-liquid interface can be either in phase, this is called "zigzag mode," or out of phase for the "varicose mode." Due to nonlinear terms, these modes may mix and a more involved pattern can arise during the temporal evolution. It is interesting to see from the linear dispersion relations that the two fluid pairs we examined both possess the zigzag type as the least stable mode. This basic pattern is also observed in the solutions presented in Sec. V of the nonlinear integrated model equations in two and three spatial dimensions.

We study three different fluid configurations. The first one is motivated by recent experiments, focusing on hydrodynamic instabilities in systems with flexible boundaries [22–24]. Pucci *et al.* have studied the response of liquid droplets floating on a viscous bath of a finite depth to external vibrations. The second is an oil-water system which is examined in detail with respect to its nonlinear pattern morphology. Beyond the well known squares or hexagons we find here intriguing localized structures that resemble large scale holes that occur roughly at the same spots at the interface and at the upper film surface.

Finally we analyze a Rayleigh-Taylor unstable stratification where the more heavy fluid (water) is located above a lighter one (oil). Although linearly unstable with respect to a wide band of growing wavelengths, we show that this system can be stabilized by vertical oscillations of the layers and rupture of one or of both of the layers which normally occurs rather soon can be avoided or at least delayed considerably.

II. NAVIER-STOKES EQUATIONS AND BOUNDARY CONDITIONS

A. System

We use the following notation: All independent (times, lengths, wave vectors, frequencies) and dependent (velocities, flow rates, pressures, layer thickness) variables bear a tilde if they have a physical dimension, otherwise they are dimensionless.

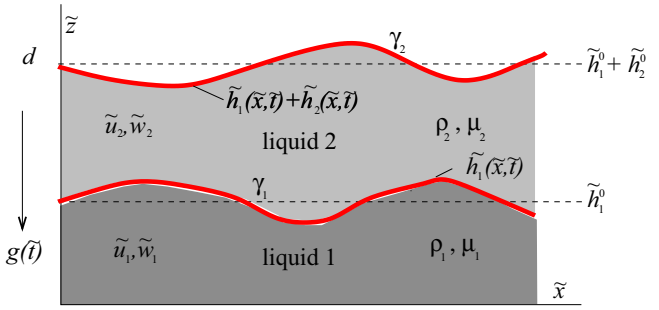

FIG. 1. Sketch of the system. Two immiscible liquids are separated by a deformable interface at $\tilde{z} = \tilde{h}_1$. The upper fluid layer has the width $\tilde{h}_2$, γ_1 denotes surface tension of the interface, γ_2 is that of the free upper surface at $\tilde{z} = \tilde{h}_1 + \tilde{h}_2$. Gravity acts in vertical direction and is time dependent due to vertical oscillations of the frame of references.

For the sake of simplicity we start with two spatial dimensions $(\tilde{x},\tilde{z})$ and generalize the treatment later to the 3D case. The system is defined in Fig. 1. If the whole setup oscillates vertically, gravity acceleration in the comoving frame reads

$$g(\tilde{t}) = g_0(1 + a\cos\tilde{\omega}\tilde{t}), \quad g_0 = 9.81\ \mathrm{m/s^2}. \tag{1}$$

In Eq. (1) two important control parameters occur, the dimensionless amplitude a, giving the acceleration in multiples of g, and the angular frequency $\tilde{\omega}$. In the work presented here we keep $\tilde{\omega}$ constant and consider a as the bifurcation parameter.

We define the dimensionless ratios of dynamic viscosities and of densities as

$$\mu = \frac{\mu_1}{\mu_2}, \quad \rho = \frac{\rho_1}{\rho_2}. \tag{2}$$

For a stable configuration one must have $\rho \geqslant 1$, otherwise the system is Rayleigh-Taylor unstable.

The undisturbed system $\tilde{h}_i = \tilde{h}_i^0 = \text{const}$ has the total depth $d = \tilde{h}_1^0 + \tilde{h}_2^0$.

B. Long-wave approximation

Let $(\tilde{u}_i,\tilde{w}_i)$ be the velocity and $\tilde{P}_i$ the pressure of a viscous and incompressible fluid in layer i, $i = 1,2$. The continuity equations and the Navier-Stokes equations in the long-wave approximation then read

$$0 = \partial_{\tilde{x}}\tilde{u}_i + \partial_{\tilde{z}}\tilde{w}_i, \tag{3}$$

$$\partial_{\tilde{t}}\tilde{u}_i + \partial_{\tilde{x}}\tilde{u}_i^2 + \partial_{\tilde{z}}\tilde{u}_i\tilde{w}_i = \nu_i\partial_{\tilde{z}\tilde{z}}^2\tilde{u}_i - \frac{1}{\rho_i}\partial_{\tilde{x}}\tilde{P}_i, \tag{4}$$

$$0 = -\frac{1}{\rho_i}\partial_{\tilde{z}}\tilde{P}_i - g(\tilde{t}) \tag{5}$$

with the kinematic viscosities $\nu_i = \mu_i/\rho_i$.

The standard way to apply the long-wave (or lubrication) approximation [25] is to assume that for the deformations of the film surface with the given wavelength $\tilde{\lambda} = 2\pi/\tilde{k} \gg d$, the ratio (Reynolds number) $\mathrm{Re}_\parallel = \tilde{u}_i d/\nu_i$ associated with the horizontal velocity $\tilde{u}_i$ is of order 1, whereas the Reynolds number of the vertical liquid motion is much smaller, $\mathrm{Re}_\perp = \tilde{w}_i d/\nu_i \sim \epsilon \ll 1$, with $\epsilon = d/\tilde{\lambda} \ll 1$ being the small parameter of the long-wave approximation. In this case, the inertial terms [left hand side of Eq. (4)] are of order ϵ and can be neglected compared to the right hand side which is of order 1. Then the resulting liquid motion appears to be described by the Stokes equation.

A different version of the long-wave approximation assumes $\mathrm{Re}_\perp = \tilde{w}_i d/\nu_i \sim 1$ together with $\tilde{u}_i \gg \tilde{w}_i$. This condition can be satisfied in liquid films subjected to external periodic vibration [19], when the viscosity ν_i is relatively small. In this limit, the inertial terms are retained, as in Eqs. (4).

The consistency of the approximation Eqs. (4) can be expressed by comparing the magnitude of the inertial term $|\partial_{\tilde{t}}\tilde{u}_i|$ with the divergence of the strain rate tensor $|\nu_i \tilde{\Delta}\tilde{u}_i|$. Namely, let us assume that the horizontal velocity $\tilde{u}_i$ oscillates with a frequency of order $\tilde{\omega}$ (harmonic or subharmonic oscillations). Then the strength of the inertial term $|\partial_{\tilde{t}}\tilde{u}_i|$ is of the order of $|\tilde{\omega}\tilde{u}_i|$. For the lubrication approximation to be valid, we require that $|\nu_i \partial^2_{\tilde{x}\tilde{x}}\tilde{u}_i|$ is negligible compared to $|\nu_i \partial^2_{\tilde{z}\tilde{z}}\tilde{u}_i|$ and, *simultaneously*, to $|\partial_{\tilde{t}}\tilde{u}_i|$. This yields $|\nu_i \partial^2_{\tilde{x}\tilde{x}}\tilde{u}_i \ll |\tilde{\omega}\tilde{u}_i|$, or, for a plane wave with wave vector $\tilde{k}$, $\tilde{k} \ll \sqrt{\tilde{\omega}/(\nu_i)}$. Note that the length parameter $\sqrt{2\nu_i/\tilde{\omega}}$ is known as the length of the acoustic boundary layer induced by the vibration of the plate [26] (the factor 2 originates from the assumption of a subharmonic oscillation of the wave).

To conclude, the consistency of the long-wave approximation leads to a set of two conditions that need to be met simultaneously for each fluid ($i = 1,2$):

$$\tilde{k} \ll \frac{1}{\tilde{l}_i} \tag{6}$$

with the acoustic boundary layer widths $\tilde{l}_i = \sqrt{2\nu_i/\tilde{\omega}}$.

C. Boundary conditions

Let us first introduce the two flow rates

$$\tilde{q}_1(\tilde{x},\tilde{t}) = \int_0^{\tilde{h}_1} d\tilde{z}\ \tilde{u}_1(\tilde{x},\tilde{z},\tilde{t}), \quad \tilde{q}_2(\tilde{x},\tilde{t}) = \int_{\tilde{h}_1}^{\tilde{h}_1+\tilde{h}_2} d\tilde{z}\ \tilde{u}_2(\tilde{x},\tilde{z},\tilde{t}). \tag{7}$$

At the bottom, we assume no-slip conditions

$$\tilde{u}_1 = 0 \quad \text{at} \quad \tilde{z} = 0. \tag{8}$$

On the interface at $\tilde{z} = \tilde{h}_1$ we have the kinematic condition

$$\partial_{\tilde{t}}\tilde{h}_1 = -\partial_{\tilde{x}}\tilde{q}_1, \tag{9}$$

the stress balance

$$\mu\partial_{\tilde{z}}\tilde{u}_1 = \partial_{\tilde{z}}\tilde{u}_2, \tag{10}$$

and the continuity for the velocity

$$\tilde{u}_1 = \tilde{u}_2, \quad \tilde{w}_1 = \tilde{w}_2. \tag{11}$$

For the pressure at the interface one finds

$$\tilde{P}_1 = \tilde{P}_2 - \gamma_1 \partial^2_{\tilde{x}\tilde{x}}\tilde{h}_1 \tag{12}$$

with the surface tension γ_1 of the interface. On the free upper surface at $\tilde{z} = \tilde{h}_1 + \tilde{h}_2$, a second kinematic condition applies,

$$\partial_{\tilde{t}}\tilde{h}_2 = -\partial_{\tilde{x}}\tilde{q}_2. \tag{13}$$

A stress-free surface implies

$$\partial_{\tilde{z}}\tilde{u}_2 = 0, \tag{14}$$

and for the pressure we finally get

$$\tilde{P}_2 = \tilde{P}_e - \gamma_2 \partial^2_{\tilde{x}\tilde{x}}(\tilde{h}_1 + \tilde{h}_2) \tag{15}$$

with the surface tension γ_2 at the free surface. The external pressure $\tilde{P}_e$ can be arbitrarily set to zero.

The lateral boundary conditions are always assumed to be periodic:

$$\tilde{u}(\tilde{x}) = \tilde{u}(\tilde{x} + \tilde{L}) \tag{16}$$

for all dependent variables, where $\tilde{L}$ is the side length. The same applies for our 3D computations with $\tilde{u}(\tilde{x},\tilde{y}) = \tilde{u}(\tilde{x} + \tilde{L}_x,\tilde{x})$, $\tilde{u}(\tilde{x},\tilde{y}) = \tilde{u}(\tilde{x},\tilde{y} + \tilde{L}_y)$.

D. Pressures

Integration of (5) gives with (12) and (15) for the pressures

$$\tilde{P}_1(\tilde{x},\tilde{z},\tilde{t}) = \rho_1 g(\tilde{t})(\tilde{h}_1 + \tilde{h}_2/\rho - \tilde{z}) - \gamma_1 \partial^2_{\tilde{x}\tilde{x}} \tilde{h}_1 - \gamma_2 \partial^2_{\tilde{x}\tilde{x}}(\tilde{h}_1 + \tilde{h}_2), \tag{17}$$

$$\tilde{P}_2(\tilde{x},\tilde{z},\tilde{t}) = \rho_2 g(\tilde{t})(\tilde{h}_1 + \tilde{h}_2 - \tilde{z}) - \gamma_2 \partial^2_{\tilde{x}\tilde{x}}(\tilde{h}_1 + \tilde{h}_2). \tag{18}$$

Equations (17) and (18) show that in the long-wave approximation, the distribution of pressure in each layer is equal to the hydrostatic pressure and therefore independent of the fluid motion.

E. Scaling and dimensionless equations

We use the scaling

$$\tilde{t} = \frac{d^2}{\nu_1} t, \quad (\tilde{x},\tilde{z},\tilde{h}_i) = d\,(x,z,h_i), \quad (\tilde{u}_i,\tilde{w}_i) = \frac{\nu_1}{d}(u_i,w_i), \quad \tilde{P}_i = \frac{\rho_1 \nu_1^2}{d^2} P_i \tag{19}$$

and find the dimensionless equations:

$$\partial_t u_1 + \partial_x u_1^2 + \partial_z u_1 w_1 = \partial^2_{zz} u_1 - \partial_x P_1, \tag{20}$$

$$\partial_t u_2 + \partial_x u_2^2 + \partial_z u_2 w_2 = \frac{\rho}{\mu}\,\partial^2_{zz} u_2 - \rho\,\partial_x P_2, \tag{21}$$

where

$$\partial_x P_1(h_i) = F(t)(\partial_x h_1 + \partial_x h_2/\rho) - \Gamma_1 \partial^3_{xxx} h_1 - \Gamma_2 \partial^3_{xxx}(h_1 + h_2), \tag{22}$$

$$\partial_x P_2(h_i) = F(t)(\partial_x h_1 + \partial_x h_2)/\rho - \Gamma_2 \partial^3_{xxx}(h_1 + h_2), \tag{23}$$

with

$$F(t) = G(1 + a\cos\omega t), \tag{24}$$

and the three dimensionless groups

$$G = \frac{g_0 d^3}{\nu_1^2}, \quad \Gamma_i = \frac{\gamma_i d}{\rho_1 \nu_1^2}, \tag{25}$$

where G is the Galileo number and Γ_i are the inverse capillary numbers.

The boundary conditions for the dimensionless variables are given by (8)–(15) with all tildes removed and with γ_i replaced by Γ_i.

F. Fluid parameters

The scaled two-layer system is thus described by the dimensionless parameters G, Γ_i, ρ, ν, the depth ratio h_1^0, the driving frequency ω, and the amplitude a. In addition, we supplement each set of parameters by the characteristic widths of the acoustic boundary layers $\tilde{l}_i = \sqrt{2\nu_i/\tilde{\omega}}$. In the following we consider three special configurations, further referred to as (A,B,C). Their fluid parameters are compiled in Table I. The dimensionless parameters and acoustic layer widths read as follows:

TABLE I. Fluid parameters of the three considered configurations. (C) is Rayleigh-Taylor unstable.

	μ_1 (Pa s)	μ_2 (Pa s)	ρ_1 (Kg/m^3)	ρ_2 (Kg/m^3)	γ_1 (N/m)	γ_2 (N/m)	d (mm)	$\tilde{h}_1^0$ (mm)	h_1^0	$\tilde{\omega}/2\pi$ (Hz)
(A)	0.026	0.0018	1850	785	0.0063	0.024	6.9	5	0.725	10
(B)	0.001	0.0046	1000	920	0.02	0.02	1.0	var.	var.	5
(C)	0.008	0.001	800	1000	0.02	0.07	1.0	0.5	0.5	10

(A) An isopropanol film deposited over an oil film, as used in the experiments by Pucci *et al.* [22], $G = 16316$, $\Gamma_1 = 119$, $\Gamma_2 = 453$, $\rho = 2.36$, $\mu = 14.4$. Acoustic length scales: $\tilde{l}_1 = 0.67$ mm, $\tilde{l}_2 = 0.27$ mm.

(B) A silicone oil layer placed over a water film, $G = 9810$, $\Gamma_1 = \Gamma_2 = 20\,000$, $\rho = 1.087$, $\mu = 0.217$. Acoustic length scales are $\tilde{l}_1 = 0.25$ mm, $\tilde{l}_2 = 0.56$ mm.

(C) A water film placed over a silicone oil layer, $G = 98.1$, $\Gamma_1 = 250$, $\Gamma_2 = 875$, $\rho = 0.8$, $\mu = 8$. Acoustic lengths scales are $\tilde{l}_1 = 0.56$ mm, $\tilde{l}_2 = 0.18$ mm.

For the nondriven system $a = 0$, the first two setups have a stable motionless flat state, whereas for (C) this state is Rayleigh-Taylor unstable.

The long-wave approximation remains valid as long as the characteristic wavelength of the perturbation $2\pi\tilde{k}^{-1}$ is much larger than both the average film thickness d and the acoustic length scales $\tilde{l}_i$, i.e., $2\pi\tilde{k}^{-1} \gg d$ and $2\pi\tilde{k}^{-1} \gg \tilde{l}_i$. As it will turn out in Sec. IV these conditions are fulfilled for all three configurations.

III. INTEGRATED LAYER APPROXIMATION

Next we derive the integrated layer model in dimensionless variables. The dimensionless model equations are then analyzed analytically and numerically for the three configurations (A,B,C). For the purpose of the direct comparison with the experimentally studied systems Refs. [22–24], we present all our results in the dimensional form by rescaling back to the dimensional physical variables.

A. Rate equations

Dynamic equations for the flow rates q_1 and q_2, defined by Eqs. (7), can be obtained by integrating Eq. (20) with respect to z over $0 \dots h_1$ and Eq. (21) over $h_1 \dots h_1 + h_2$. By taking into account the boundary conditions Eqs. (8), (11) and (14) and the following kinematic conditions at the moving interfaces:

$$\begin{aligned} 0 &= \partial_t h_1 + u_1(h_1)\partial_x h_1 - w_1(h_1), \\ 0 &= \partial_t(h_1 + h_2) + u_2(h_1 + h_2)\partial_x(h_1 + h_2) - w_2(h_1 + h_2), \end{aligned} \tag{26}$$

we obtain after some manipulations

$$\partial_t q_1 + \partial_x\langle u_1^2\rangle = \partial_z u_1|_{z=h_1} - \partial_z u_1|_{z=0} - h_1\partial_x P_1, \tag{27}$$

$$\partial_t q_2 + \partial_x\langle u_2^2\rangle = -\frac{\rho}{\mu}\,\partial_z u_2|_{z=h_1} - h_2\rho\partial_x P_2 \tag{28}$$

with

$$\langle u_1^2\rangle = \int_0^{h_1} dz\, u_1^2, \quad \langle u_2^2\rangle = \int_{h_1}^{h_1+h_2} dz\, u_2^2. \tag{29}$$

The two equations (27) and (28) together with the pair (9) and (13) form a set of coupled nonlinear partial differential equations for q_1, q_2, h_1, h_2 in x, t, so the spatial dimension of the original problem is reduced by 1.

We emphasize that the four equations (9), (13), (27), and (28) contain six field variables, namely the rates q_i, the horizontal fluid velocities u_i, and the thicknesses of the layers h_i. In addition, the rates q_i are linked to the velocities u_i via (7). However, due to the presence of the quadratic terms $\partial_x\langle u_i^2\rangle$, the system of six equations is not closed, as it does not contain the dynamic equations for the velocities u_i. In order to close the nonlinear system one needs to establish an additional relation between the instantaneous values of u_i and the rates q_i. In the next section we make further assumptions on the z dependence of the velocities u_i and derive the closed set of four dynamic equations for q_i and h_i in the so-called *integrated layer approximation*.

Remarkably, however, if the set of equations (9), (13), (27), and (28) is linearized about the motionless steady state, given by $u_i = 0$ and $h_1 = h_1^0$, $h_2 = 1 - h_1^0$, the quadratic terms $\partial_x\langle u_i^2\rangle$ vanish and the system can be solved analytically, using the plane wave ansatz, as shown in detail in Appendix B. The corresponding solution is further referred to as the full (or nonreduced) long-wave approximation.

B. Closure: Polynomials

In this section we relate the flows q_i to the velocities u_i and to the profiles h_i. As the closure approximation, we are using the quasistationary version of the long-wave approximation, according to which the inertial terms are neglected as compared with the viscous strain tensor $\nu\Delta u_i$ [27]. The resulting Stokes equations can be integrated to yield a quadratic z dependence of the horizontal velocities $u_i(z)$. Namely, we use for $u_i(z)$ the ansatz

$$\begin{aligned} u_1 &= \Phi_1(z^2 - 2zh_1) - \Phi_2 h_2 z, \\ u_2 &= \tfrac{1}{2}\mu\Phi_2[(z-h_1)^2 - 2h_2(z-h_1)] - \Phi_1 h_1^2 - \Phi_2 h_1 h_2 \end{aligned} \tag{30}$$

that automatically fulfills the boundary conditions (8), (10), (11), (14) for two independent functions $\Phi_i(x,t)$. Approximation (30) remains valid as long as the driving frequency ω is small, implying relatively slow (quasistationary) flow fields. It is exact for the case of vanishing Reynolds number.

Inserting (30) into (7) yields a linear dependence between Φ_i and q_i of the form

$$\Phi_i = \sum_j M_{ij}(h_i)\, q_j \tag{31}$$

that can be inserted into (30) and then into (27) and (28) and that closes the system. The explicit form of $\underline{M}$ can be found in the Eq. (A1) in Appendix A.

IV. LINEAR STABILITY

A. Linearized model system

The motionless base state

$$u_i = q_i = 0 \tag{32}$$

has a flat surface and a flat interface located at $z = h_1^0$ and at $z = h_1^0 + h_2^0 = 1$, respectively, so there remains only one free geometry parameter, say h_1^0. With the closure polynomials (30), Eqs. (27), (28), (9), and (13) can be linearized about the base state to give a system of four linear partial differential equations with time periodic coefficients for $q_i(x,t)$ and $\eta_i(x,t)$:

$$\partial_t q_1 = \frac{2h_1^0}{D(h_i^0)}\left[-(h_2^0)^2\left(\frac{\mu h_2^0}{3} + h_1^0\right)q_1 + \frac{h_2^0(h_1^0)^2}{2}q_2\right] - h_1^0\partial_x P_1(\eta_1,\eta_2,t), \tag{33}$$

$$\partial_t q_2 = \frac{\rho h_2^0}{D(h_i^0)}\left(h_2^0(h_1^0)^2 q_1 - \frac{2(h_1^0)^3}{3}q_2\right) - \rho h_2^0\partial_x P_2(\eta_1,\eta_2,t), \tag{34}$$

$$\partial_t \eta_1 = -\partial_x q_1, \tag{35}$$

$$\partial_t \eta_2 = -\partial_x q_2, \tag{36}$$

where

$$\eta_i = h_i - h_i^0 \tag{37}$$

and $D = (\det \underline{M})^{-1}$ [see Eq. (A2)]. The system (33)–(36) is referred to as the linearized integrated layer approximation.

Space dependence is removed by Fourier transformation

$$q_j(x,t) = q_j^k(t)\exp(-ikx), \quad \eta_j(x,t) = \eta_j^k(t)\exp(-ikx). \tag{38}$$

By the help of the substitution

$$\vec{Y}(t) = \left(q_1^k(t), q_2^k(t), i\eta_1^k(t), i\eta_2^k(t)\right), \tag{39}$$

(33)–(36) can be written in the form of four real valued ordinary differential equations,

$$d_t \vec{Y} = \left[\underline{A}\left(h_i^0\right) + \underline{B}\left(h_i^0, t\right)\right]\vec{Y} \tag{40}$$

with the 4×4 matrices $\underline{A}$, $\underline{B}$ given in Eqs. (A3) and (A4).

B. Floquet analysis: Numerical results

Since $\underline{B}(t) = \underline{B}(t+T)$ with $T = 2\pi/\omega$, Floquet's theorem applies and the solution of (40) reads

$$\vec{Y}(t) = \sum_{j=1}^{4} e^{\Lambda_j t}\vec{\chi}_j(t) \tag{41}$$

with

$$\vec{\chi}_j(t) = \vec{\chi}_j(t+T). \tag{42}$$

The Floquet exponents Λ_j can be computed from the eigenvalues σ_j of the monodromy matrix $\underline{Q}$ defined as $\vec{Y}(t+T) = \underline{Q} \cdot \vec{Y}(t)$, according to

$$\Lambda_j = \frac{1}{T}\ln \sigma_j. \tag{43}$$

The monodromy matrix is determined by integrating (40) numerically with a standard fourth order Runge-Kutta scheme over one period T for the four orthogonal initial conditions

$$\vec{Y}_i(0) = \hat{e}_i \tag{44}$$

with the unit vectors $\hat{e}_1 = (1,0,0,0)$, etc. The vectors $\vec{Y}_i(T)$ then form the columns of $\underline{Q}$. If at least one of the Floquet exponents has a positive real part ($|\sigma_i| > 1$), the motionless base state (32) is unstable and Faraday patterns may occur. The stability threshold, computed from the integrated layer approximation (40), is compared with the exact solution of the nonreduced linearized long-wave equations (A2). Additionally, we compare the approximate results with the exact stability threshold, found from the linearized full Navier-Stokes equations [21].

We first compute the zeros of the real part of the largest Floquet exponent for setups (A,B) defined in Sec. II F in the $\tilde{k} - a$ plane (Fig. 2). To this purpose we go back to dimensionalized quantities. Although the instability which occurs in configuration (A) is not clearly long wave ($\tilde{k}_c \approx 0.1/\text{mm}$ corresponds to $\tilde{\lambda}_c \approx 63$ mm, the total depth of the layer is in the range of 7 mm), we use it here for comparison with the computations done recently in Ref. [21] on exact solutions of the linearized two-layer system.

Configuration (B) fulfills the long-wave assumption much better since the layer depths are less than 1 mm. Then even the second and third tongues show wavelengths which are at least by a factor

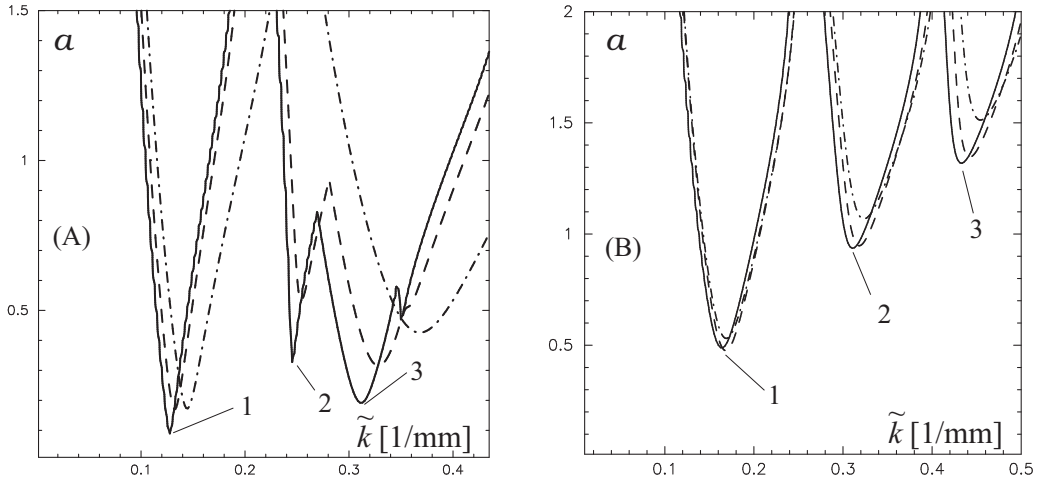

FIG. 2. Amplitude a from (1) of vertical vibrations over wave vector $\tilde{k}$ from (38). Left: Stability map for configuration (A) and $\tilde{\omega}/2\pi = 10$ Hz. The first (counting from the left) and the third tongues correspond to a subharmonic excitation ($\sigma = -1$), the second, smaller one, to a harmonic one ($\sigma = 1$). Solid lines: Integrated layer model; dashed: long-wave approximation, dashed-dotted: linearized Navier-Stokes equations without further approximations. Right: Same for configuration (B) and $\tilde{\omega}/2\pi = 5$ Hz, $\tilde{h}_1^0 = 0.5$ mm.

15 larger than the depths. As in the standard one-layer Faraday problem, the tongues in alternation correspond to subharmonic and harmonic excitations. Increasing the depths ratio h_1^0 decreases both wave number and threshold of each tongue.

Also in Fig. 2 we demonstrate the agreement of the linear results between full Navier-Stokes equations [21], lubrication approximation with inertia, see Appendix B, and the integrated model. As expected, the deviations of the approximations from the Navier-Stokes equations become larger for increasing $\tilde{k}$, but the first (unstable) tongue fits quite well.

In configuration (C) the heavier fluid is placed on top, rendering the nonvibrating system gravitationally unstable (Rayleigh-Taylor instability, RTI) for [28]

$$0 < |\tilde{k}| < \tilde{k}_0 = \frac{1}{d}\sqrt{\frac{G}{\Gamma_1}\left(\frac{1}{\rho} - 1\right)} = \sqrt{\frac{g_0(\rho_2 - \rho_1)}{\gamma_1}} \approx 0.315 \text{ mm}^{-1} \tag{45}$$

and normally rupture occurs in the nonlinear regime. Note that in contrast to the classical RTI where the heavier fluid sits under a rigid wall, in our case the heavier fluid has a deformable surface on both sides. So rupture may occur either when the interface touches the free surface or when the heavier fluid reaches the solid substrate.

From Fig. 3 one may conclude that Faraday vibrations narrow the RTI region only very weakly (slight inclination of the vertical line starting at $\tilde{k}_0$). For larger values of $\tilde{k} > \tilde{k}_0$ Faraday unstable branches occur and destabilize the system even further. However, as we shall show below, the fully nonlinear model yields a saturation of spatially periodic patterns without rupture in the long-time limit for intermediate values of the acceleration a.

C. Dispersion relation

For the unforced system $a = 0$, $\underline{B} = 0$, (40) does not depend explicitly on time. Then $\vec{Y}(t) \sim \exp(\Lambda_i t)$, where Λ_i are the four eigenvalues of the system matrix $\underline{A}$ of (40), which can be computed by a standard routine, e.g., DGEEV from LAPACK [29]. Real and imaginary parts of Λ_i denote growth rate and frequency of a plane wave and can be plotted over the wave vector, showing the

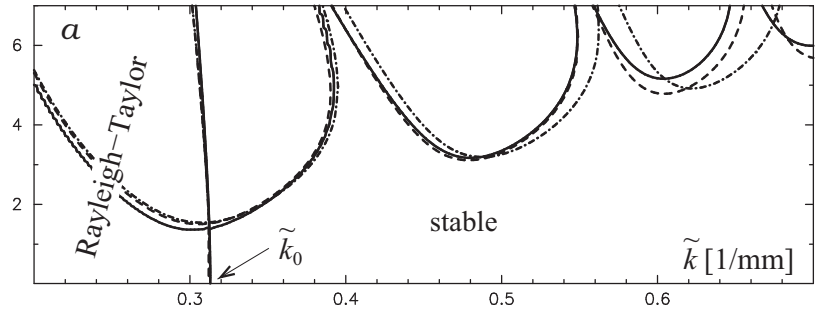

FIG. 3. Configuration (C) is Rayleigh-Taylor unstable in the region left from the slightly inclined vertical line starting at $\tilde{k} = \tilde{k}_0$, $a = 0$. Solid lines: Integrated layer model; dashed: long-wave approximation; dashed-dotted: full Navier-Stokes equations.

dispersion relation (Figs. 4 and 5). Since there is no instability mechanism in the nondriven system, all growth rates must be negative.

From a certain finite $\tilde{k}$ on the surface waves are dispersive with a nonzero oscillation frequency $\tilde{\Omega} \neq 0$. Two monotonically rising branches in the right frames in Figs. 4 and 5 correspond to the zigzag and the varicose thinning modes, as marked by "z" and "v," respectively. The deformations of the film surface and the liquid-liquid interface are in phase for the zigzag mode and out of phase for the varicose mode. For configurations (A) and (B) the least stable mode is of the zigzag type. Dispersion relations of the zigzag and the varicose modes in the vibration-free system was systematically studied in Ref. [21]. It was shown that in the case when the interfacial tension γ_1 is significantly decreased, the more stable varicose mode shows anomalies in the dispersion relation. Here, for parameters as in (A) and (B), both surface modes have normal dispersion relation with positive group velocity $d\tilde{\Omega}/d\tilde{k} > 0$.

The squares on the right frames in Figs. 4 and 5 correspond to wave vectors that minimize the critical amplitude of the driven system discussed in Sec. IV B. The computed frequencies found

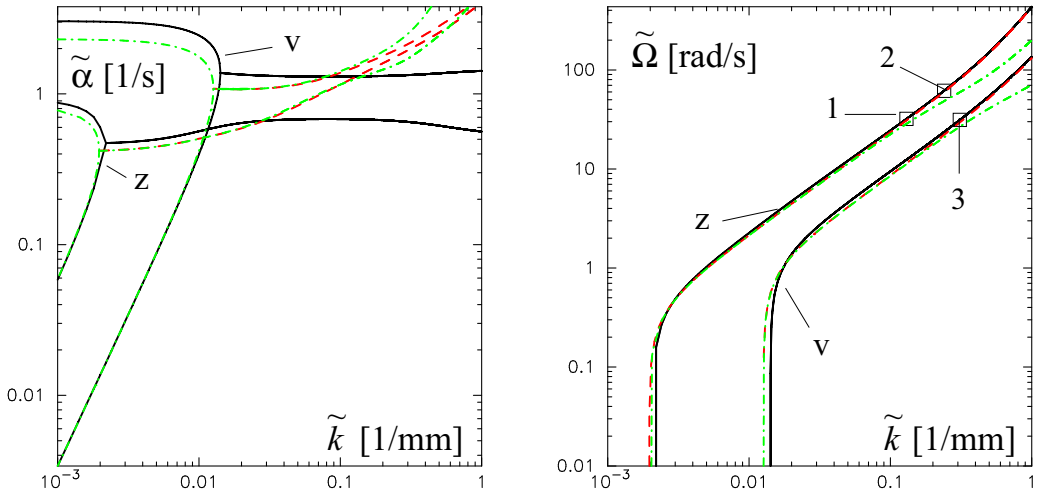

FIG. 4. Negative growth rate $\tilde{\alpha} = -\mathrm{Re}(\tilde{\Lambda})$ (left) and frequency $\tilde{\Omega} = \mathrm{Im}(\tilde{\Lambda})$ (right) over the wave number $\tilde{k}$ for configuration (A). The rectangles correspond to the minima of the critical lines in Fig. 2, left frame. Solid (black): integrated model; dashed (red): Navier-Stokes, long-wave; dashed-dotted (green): full Navier-Stokes. The labels "z" and "v" denote zigzag and varicose mode types (see text).

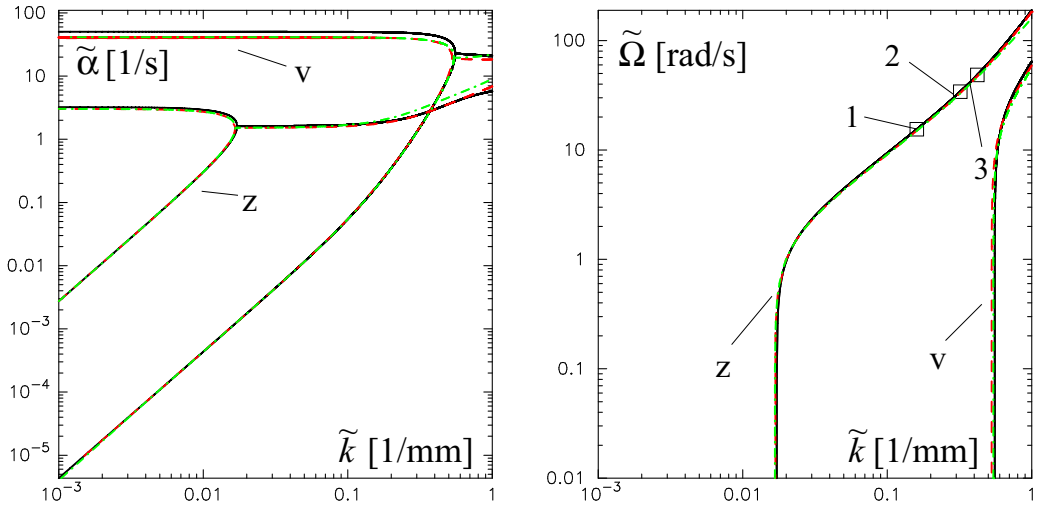

FIG. 5. Same as Fig. 4 but for configuration (B), $\tilde{h}_1^0 = 0.5$ mm.

from Fig. 4 are

$$\tilde{\Omega}_1 = 32 \text{ rad/s}, \quad \tilde{\Omega}_2 = 62 \text{ rad/s}, \quad \tilde{\Omega}_3 = 31 \text{ rad/s}.$$

This agrees quite well with the driving frequency of $\tilde{\omega} = 10 \times 2\pi$ rad/s, respectively the half frequency for the two subharmonic branches. It is interesting that the third tongue is linked to the excitation of the more stable eigenvalue.

The same agreement is obtained for configuration (B). Here, the second pair of eigenvalues forms a conjugate complex pair only for larger values of k and the tips of the first three tongues all lay on the less stable branch. The frequencies detected from Fig. 5, right frame, read

$$\tilde{\Omega}_1 = 15 \text{ rad/s}, \quad \tilde{\Omega}_2 = 33 \text{ rad/s}, \quad \tilde{\Omega}_3 = 46 \text{ rad/s},$$

corresponding to half, integer, and three half of the driving frequency.

We point out the almost perfect agreement between the integrated layer approximation on one hand, and the full Navier-Stokes equations on the other hand, for configuration (B), as shown in Fig. 5.

V. NONLINEAR MODEL AND NUMERICAL SOLUTIONS

A. One horizontal dimension

The fully nonlinear set of integrated basic equations (27), (28), (9), and (13) has the dimension (1+1) and can be reformulated as

$$\partial_t q_1 + \partial_x \langle u_1^2 \rangle = \sum_{j=1}^{2} A_{1,j}(h_i) q_j - h_1 \partial_x \big[F(t)(h_1 + h_2/\rho) - \Gamma_1 \partial_{xx}^2 h_1 - \Gamma_2 \partial_{xx}^2 (h_1 + h_2) \big],$$

$$\partial_t q_2 + \partial_x \langle u_2^2 \rangle = \sum_{j=1}^{2} A_{2,j}(h_i) q_j - h_2 \partial_x \big[F(t)(h_1 + h_2) - \rho \Gamma_2 \partial_{xx}^2 (h_1 + h_2) \big], \tag{46}$$

$$\partial_t h_1 + \partial_x q_1 = 0,$$

$$\partial_t h_2 + \partial_x q_2 = 0. \tag{47}$$

Using (29) with (30), one finds

$$\langle u_1^2\rangle = \frac{h_1^3}{3}\left(\frac{8}{5}h_1^2\Phi_1^2 + h_2^2\Phi_2^2 + \frac{5}{2}h_1h_2\Phi_1\Phi_2\right),$$
$$\langle u_2^2\rangle = h_1^4h_2\Phi_1^2 + \frac{2}{3}h_2^3\Phi_2^2\left(\frac{1}{5}\mu^2h_2^2 + \mu h_1h_2 + \frac{3}{2}h_1^2\right) + 2\Phi_1\Phi_2h_1^2h_2^2\left(h_1 + \frac{1}{3}\mu h_2\right). \quad (48)$$

Inserting Φ_i from (31) finally closes the system.

B. Numerical solutions

We integrate (46) and (47) with an FTCS method (forward time centered space) of $O(\Delta t)$ in time and $O(\Delta x^2)$ in space [30]. The step size Δx is chosen so that the critical wavelength of the first tongue is resolved with 15 mesh points. The time step is less than $10^{-4}T$. Through all the following runs, periodic lateral boundary conditions are assumed (see Sec. II C). As initial condition ($t = 0$) a random perturbation of the flat motionless state

$$h_1(x_i,0) = h_1^0 + 0.1\,\xi_i, \quad h_2(x_i,0) = h_2^0 + 0.1\,\xi_i, \quad q_1(x_i,0) = q_2(x_i,0) = 0 \quad (49)$$

applies. Here, $x_i = i\,\Delta x$ is the location of grid point i and ξ_i denote equally distributed independent random numbers in $[-0.5,0.5]$.

1. *Gravitationally stable stratification*

We start with set (A), Fig. 6, top panel. At the very early stage of the time evolution $\tilde{t} < 8$ s, the zigzag mode with the spatial period of ≈52 mm is formed (not shown). The mode oscillates with the half of the driving frequency, i.e., at 5 Hz. This is in perfect agreement with the linear stability analysis, as shown in the left panel of Fig. 2. It can be seen that the tip of the first subharmonic tongue corresponds to a zigzag mode with $\tilde{k} = 0.12\ \mathrm{mm}^{-1}$, giving rise to the wavelength of $2\pi/\tilde{k} = 52$ mm.

However, for $\tilde{t} > 8$ s, a second zigzag mode with the wavelength of ≈25 mm develops and overlays the primary mode. The oscillation frequency of the second mode is close to the driving frequency of 10 Hz. The resulting persisting pattern resembles an oscillating zigzag mode with a half of the primary instability wavelength, as shown in the upper panel in Fig. 6 for $\tilde{t} = 68$ s. Remarkably, the temporal spectral content of the oscillating pattern contains three different frequencies, as also shown in Fig. 6, where we plot the magnitude of the Fourier transform of $\tilde{h}_1(\tilde{x}_0,\tilde{t})$ for a selected point $\tilde{x}_0$ in the middle of the domain. The major component oscillates at 5 Hz (subharmonic), whereas the other two equally strong minor components oscillate at 10 and 15 Hz, respectively.

As a possible explanation of the observed patterns we mention the nonlinear (quadratic) coupling between two zigzag modes from the tip of the first (subharmonic) tongue in Fig. 2 with the wavelength of 52 mm.

The results may be compared with the experiments from Pucci *et al.* [22–24]. However, in our case the frequency has been chosen much smaller to stay in the long-wave regime. From Fig. 4 in Ref. [22] we extract a critical wavelength of $\tilde{k} \approx 3.7/\mathrm{mm}$. In Ref. [21], we found an approximately linear relation between wave number and frequency. Assuming a linear dependence also here, this would lead to $\tilde{k} \approx 0.3/\mathrm{mm}$ in our case, a value that fits the shorter waves of Fig. 6 (top) quite well.

System (B) shows qualitatively the same behavior as (A) for a thin top layer (Fig. 6, third frame) with $h_1^0 = 0.8$. However, if the lower layer is rather thin, interesting localized solutions are found for isolated values of a (lower frame), $h_1^0 = 0.2$. Although the shape of the whole structure remains almost time periodic, the two edges besides the hump of the interface become thinner and thinner on a very slow time scale, leading finally to rupture in the lower layer at $\tilde{t} \approx 2700$ s.

2. *Rayleigh-Taylor unstable stratification: Delay of film rupture and stabilization of Faraday waves*

As expected, setup (C) shows RTI for $a = 0$ (Fig. 7 top). After $\tilde{t} \approx 53$ s, the interface touches the free upper surface and the top layer ruptures first. Using the periodicity length from Fig. 7 top, we

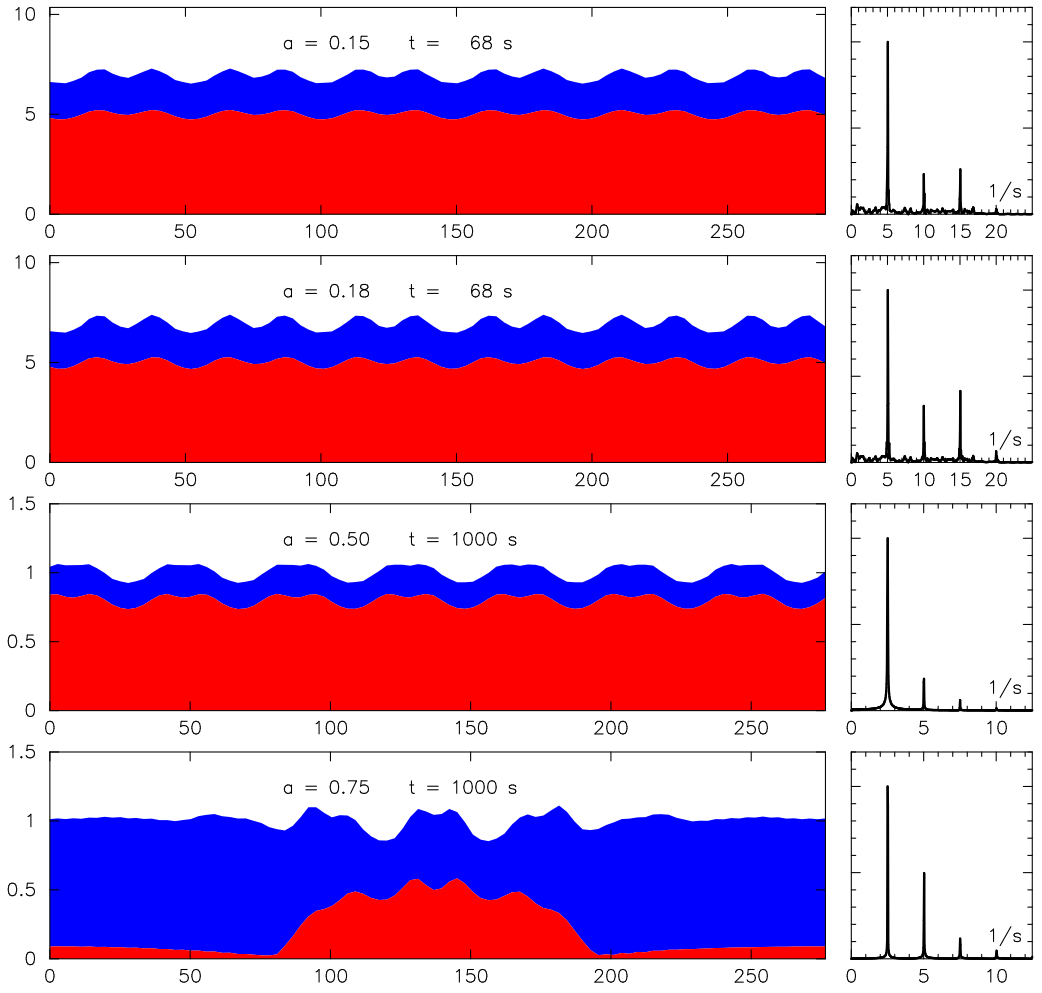

FIG. 6. Reduced 1D solutions for a 2D system, saturated or almost saturated structures. Upper two frames correspond to (A), lower ones to (B). If the lower layer is very thin, a localized solution is obtained. The last frame is not completely periodic in $2T = \pi/\omega$; see text. Vertical and horizontal units are in mm, the used value of the vibration amplitude a (multiple of g) is given in each panel. All patterns are obtained starting with the random initial condition (49). The four smaller frames on the right show the moduli of the Fourier transforms (arbitrary units) of $\tilde{h}_1(\tilde{x}_0,\tilde{t})$ for $\tilde{x}_0$ in the middle of the layer.

find $\tilde{k} \approx 0.21/\text{mm}$, a value that corresponds quite well to the fastest growing mode of the RTI (not shown).

Some older experiments show the stabilization of a flat interface of a Rayleigh-Taylor unstable two-layer system by vertical vibrations [31]. Later on a theoretical study demonstrated that both interfacial tension and viscosity are necessary for stabilization [32]. A long-wave RTI system was studied in [33] by means of a linear stability analysis. As in Fig. 3, it was found that the linear unstable RTI region is narrowed due to normal vibrations. In our case we could not find a complete stabilization of a flat interface and/or surface. However, it is interesting to see that the process of rupture is retarded if (not too strong) normal vibrations are switched on (second frame). For $a = 1.5$, the shape of the interfaces is almost identical to that of $a = 0$ but the top layer now ruptures at $\tilde{t} \approx 135$ s. Finally, for larger values of a rupture is strongly delayed or even completely avoided and large amplitude Faraday waves seem to stabilize the Rayleigh-Taylor unstable system. The

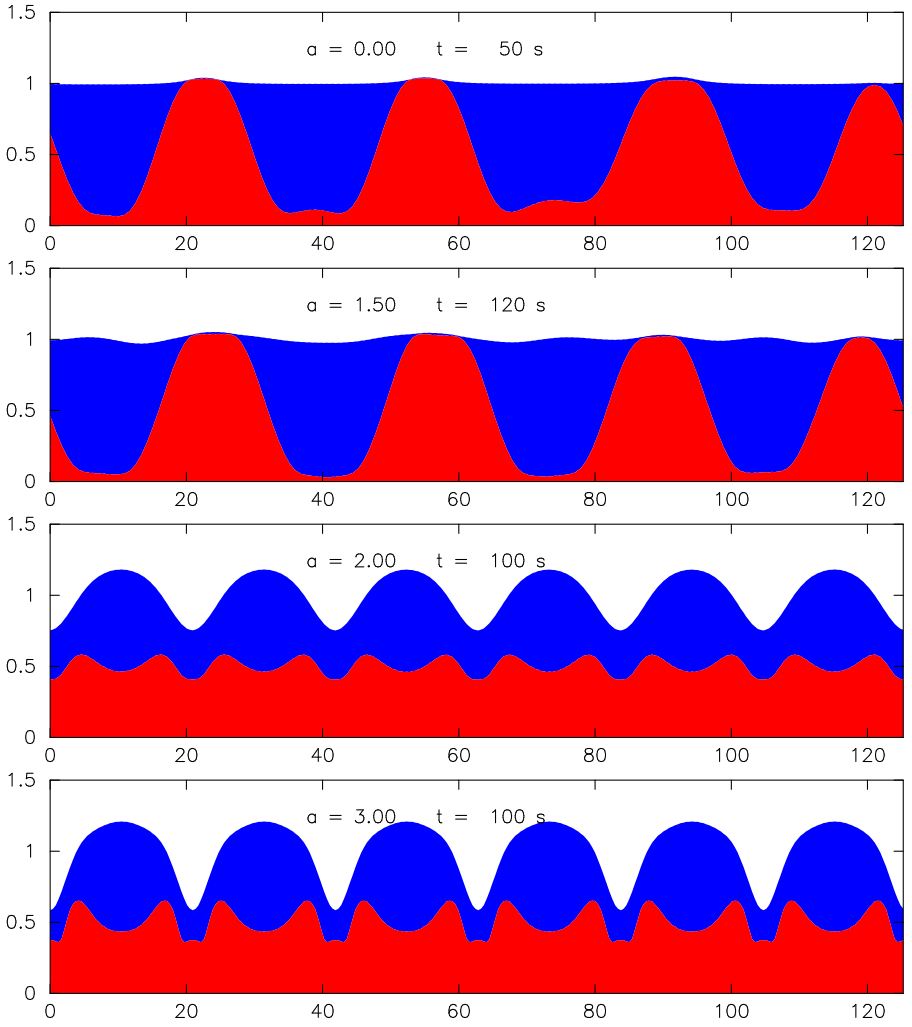

FIG. 7. Same as Fig. 6 but now for the RTI unstable configuration (C) with the heavier liquid on top. Rupture of the upper layer occurs only for small or vanishing a (first two frames), for larger values of a, a saturated periodic pattern occurs.

wave vector is now $\tilde{k} \approx 0.33$ and lies outside the RTI region right of the almost vertical line in Fig. 3. Also the interface shows even much shorter waves well inside the stable areas of Fig. 3. It seems that a stabilization via shorter waves of the RTI unstable setup (C) is achieved. Note that in the case of vanishing or small vibrations below the stabilization limit the surface remains almost completely flat over the whole process and only the interface is strongly deformed until rupture occurs.

C. Two horizontal dimensions

The treatment can be easily extended to two horizontal dimensions, describing a 3D two-layer film. The quantities u_i, Φ_i, and q_i turn into 2D vectors:

$$\vec{u}_i = \left(u_i^x(x,y,t), u_i^y(x,y,t)\right), \tag{50}$$

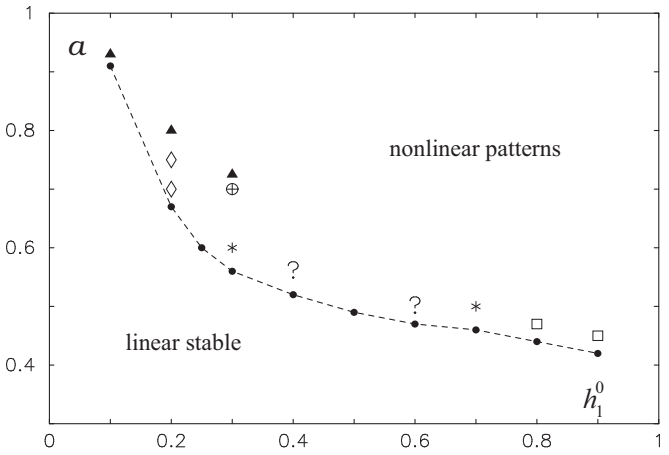

FIG. 8. Patterns found in 3D for setup (B). Dots: linear stability; squares: squares; asterisks: hexagons; triangles: rupture; diamonds: confined states [see Figs. 6 and 10]; cross in circle: quasiperiodic, supersquares; question marks: irregular.

etc. Instead of (46) and (47) one obtains the six equations

$$\partial_t \vec{q}_1 + \nabla \cdot \underline{Q}_1 = \sum_{j=1}^{2} A_{1,j}(h_i)\vec{q}_j - h_1 \nabla[F(t)(h_1 + h_2/\rho) - \Gamma_1 \nabla^2 h_1 - \Gamma_2 \nabla^2 (h_1 + h_2)],$$

$$\partial_t \vec{q}_2 + \nabla \cdot \underline{Q}_2 = \sum_{j=1}^{2} A_{2,j}(h_i)\vec{q}_j - h_2 \nabla[F(t)(h_1 + h_2) - \rho\Gamma_2 \nabla^2 (h_1 + h_2)], \tag{51}$$

$$\partial_t h_1 + \nabla \cdot \vec{q}_1 = 0,$$

$$\partial_t h_2 + \nabla \cdot \vec{q}_2 = 0, \tag{52}$$

where ∇ is the horizontal nabla and the matrices $\underline{Q}_i$ are stated in Eq. (A6).

D. Numerical solutions

The numerical scheme used in Sec. V B can be easily extended to two spatial dimensions. The CPU time using small computers like desktops or work stations is still in a reasonable range between some hours and some days, depending on the spatial resolution and parameter sets.

Again, lateral boundary conditions are assumed to be periodic now in x and y (see Sec. II C). The random initial condition (49) is extended naturally to two horizontal dimensions.

1. Gravitationally stable stratification

Localized structures and persisting oscillating patterns that appear on the surface of vertically vibrated viscous films have attracted much attention over the last two decades. Faraday waves, excited by one- and two-frequency forcing in one-layer liquid films, exhibit a rich variety of stable patterns, ranging from regular squares, hexagons, and stripes to less regular superlattice and quasiperiodic patterns and completely irregular chaotic patterns [8,34–38]. The main objective of the section is to give a brief overview of stable patterns in two-layer films, without giving an exhausting analysis.

We first show some typical patterns for configuration (B) for vibration amplitudes a close to linear threshold and for various values of the layers depth ratio h_1^0; Fig. 8. The numerical grid size varies from 100×100 up to 200×200 mesh points, the step width is $\Delta x = 2\pi/2.4 \approx 2.62$ leading to aspect ratios (length/total depth) of ≈260–520. As a main result, regular squares are found for large values of h_1^0, hexagons, however, not so regular, for smaller ones, Fig. 9. There also exists a

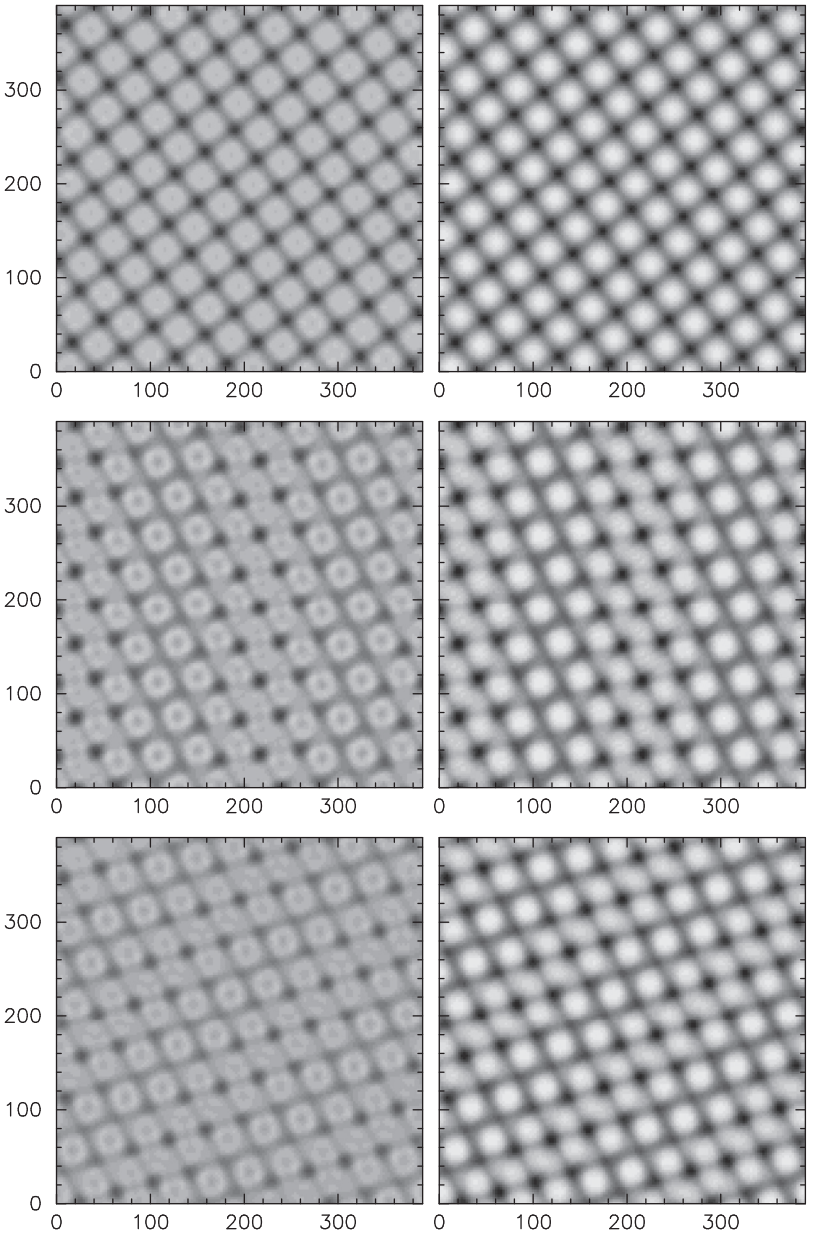

FIG. 9. Numerically computed snapshots on a 150×150 FD-grid. Shown are the interface deformations $h_1 - h_1^0$ (left frames) and the surface deformations $h_1 + h_2 - 1$ (right frames). Gray scale from maximum (black) to minimum (white) in the same scaling for both layers. For $a = 0.47$, $h_1^0 = 0.8$ one clearly observes quite regular squares, top row. For $a = 0.5$, $h_1^0 = 0.7$. the tendency to, however, not quite homogeneous hexagons is visible, middle row. For $a = 0.5$, $h_1^0 = 0.6$, more irregular squares are observed (bottom row). The unit of the axes is mm.

large region where patterns are an irregular mixture of squares and hexagons already close to onset (question marks in Fig. 8).

For higher acceleration amplitude, patterns become more and more irregular and rupture is obtained. Rupture comes sooner if one of the layers is rather thin. Then the thinner layer ruptures

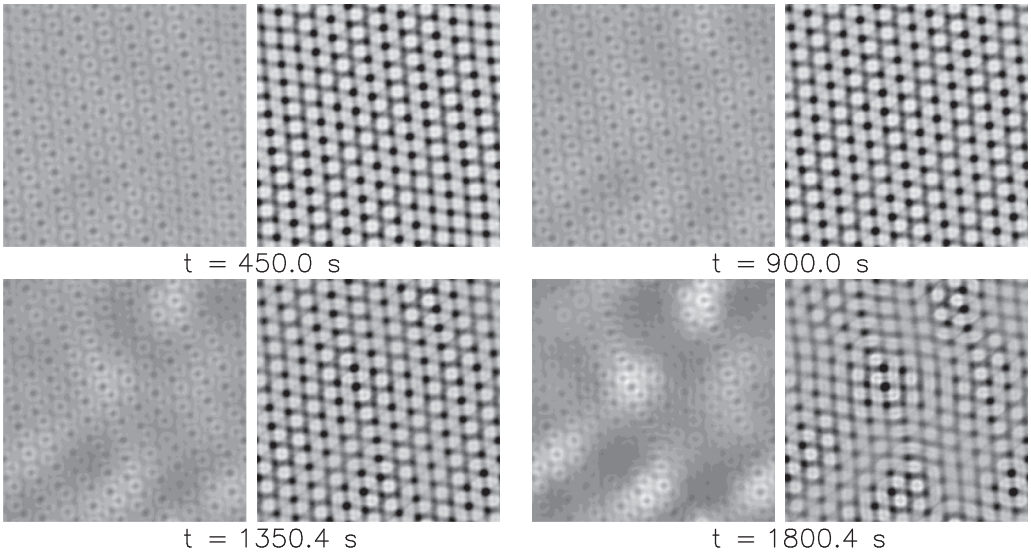

FIG. 10. Time series of configuration (B) on a 200 × 200 mesh points grid for $a = 0.7$, $h_1^0 = 0.2$. Very slowly, a depleted, finally almost flat zone occurs first in the interface (left frames), later in the surface (right frames). Side length of the layer is 524 mm.

first. If one of the layers ruptures, discontinuities occur. The long-wave model is no longer valid and computations have to be stopped.

In two dimensions (Fig. 6) we obtained localized states for $a = 0.75$, $h_1^0 = 0.2$. The same is found in three dimensions, Fig. 10. After a very long evolution time of $\tilde{t} \approx 1300$ s compared to the oscillation period of 0.2 s, a depleted region occurs first in the interface, then later at the surface.

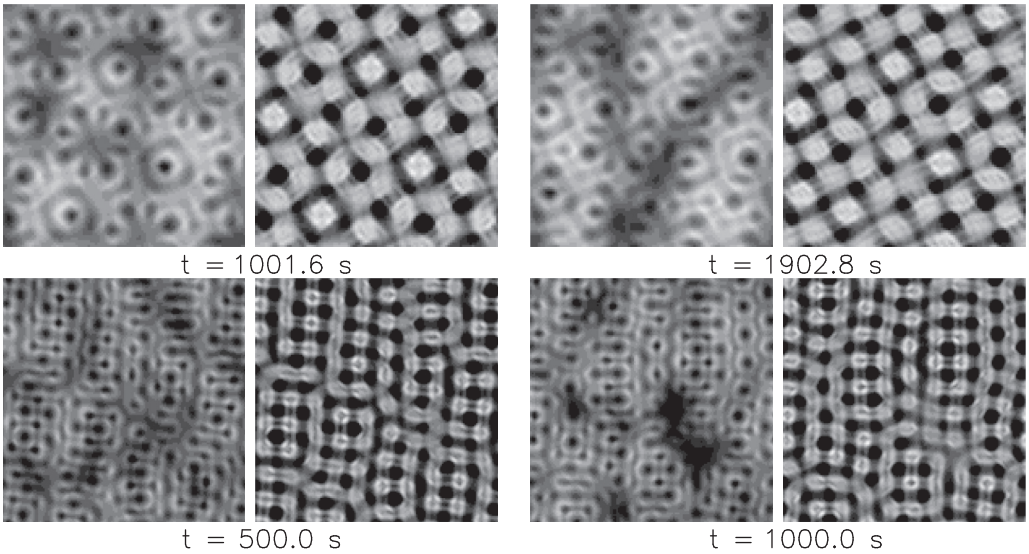

FIG. 11. Top: An eightfold (quasiperiodic) symmetry. Pattern obtained for $h_1^0 = 0.3$, $a = 0.7$ on a 100 × 100 grid, side length 262 mm. Bottom: For a larger aspect ratio of 393 mm, so-called supersquares (see text) are formed at the same parameters but on a 150 × 150 grid. For larger times, a depleted zone occurs as in Fig. 10.

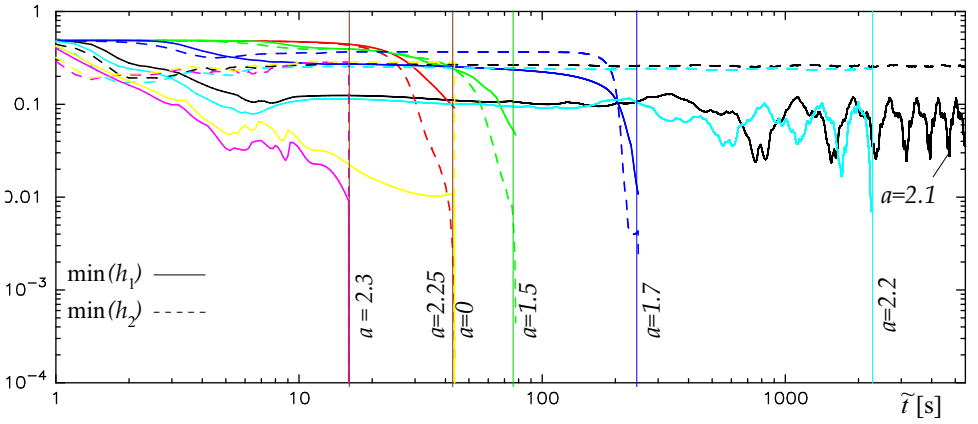

FIG. 12. min(h_1) (solid) and min(h_2) (dashed) over time of the RTI unstable configuration (C). Rupture time $\tilde{t}^*$ can be delayed if Faraday oscillations are turned on. We found for $a = 0$, $\tilde{t}^* = 44$ s (red), for $a = 1.5$, $\tilde{t}^* = 78$ s (green), for $a = 1.7$, $\tilde{t}^* = 249$ s (blue), for $a = 2.2$, $\tilde{t}^* = 2260$ s (light blue), for $a = 2.25$, $\tilde{t}^* = 43.5$ s (yellow), and for $a = 2.3$, $\tilde{t}^* = 16$ s (violet). For $a = 2.1$, rupture was not observed within the computed time $\tilde{t} < 5500$ s.

Rupture is not obtained within the computed time interval, but due to the very slow dynamics we cannot exclude rupture at later times. Considering Fig. 10, the patterns resemble the so-called oscillons reported in Ref. [39], Figs. 2(c) and 2(d) there. However, the oscillons were obtained in a one-layer system but with an excitation of two frequencies having the ratio 55/60 and 60/40, respectively.

Another interesting parameter set is $a = 0.7$, $h_1^0 = 0.3$. For a relatively small aspect ratio we find a kind of quasiperiodic structure in space which is almost time periodic over a rather long

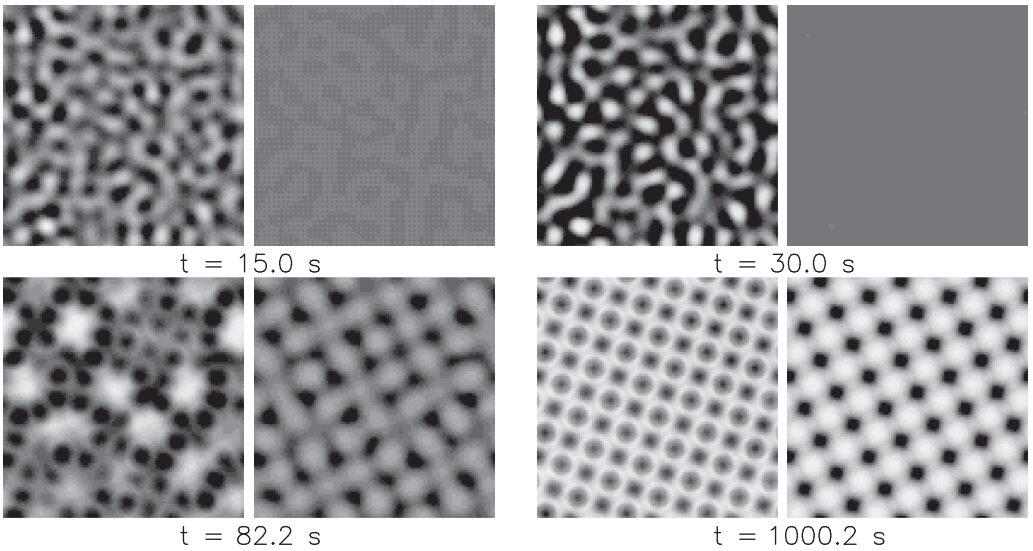

FIG. 13. Top row: two snapshots of a typical RTI, configuration (C) with $a = 0$. The upper surface remains almost completely flat. Rupture occurs after $\tilde{t} \approx 44$ s. Bottom left: for $a = 1.5$ rupture is delayed and squares are obtained, now also in the upper surface, before rupture at $\tilde{t} \approx 84$ s. Bottom right: for $a = 2.1$ no rupture is observed and a very regular square pattern occurs in both of the interfaces. Side length 140 mm, 100×100 mesh points.

time; Fig. 11. On a larger grid (150 × 150) a pattern occurs that resembles the recently numerically detected and there so-called "supersquares" in a one-layer large aspect ratio system [17]. Both supersquares and quasiperiodic structures change again on a very slow time scale, leading finally to a depleted region as in Fig. 10.

2. Rayleigh-Taylor unstable stratification

In Fig. 7 we found that a RTI unstable system can be stabilized if the oscillation amplitude is large enough. The same is true in three dimensions; at least the system can be stabilized over a very long evolution time up to almost 100 min for setup (C). To demonstrate this we plot the minimal depths $\min(h_1)$, $\min(h_2)$ over time in Fig. 12 until rupture in one of the layers occurs. For $a = 0$ or not too large a, the upper layer ruptures first. For larger a the stabilization phase becomes longer and longer. There seems to be a point of culmination around $a = 2.1$ from that on rupture again occurred sooner, but now first in the lower layer. During the stabilization, both surfaces are organized in the form of regular square patterns.

In contrast, purely RTI driven pattern formation ($a = 0$) shows quite irregular surface structures (Fig. 13). Mainly the lower surface is modulated; it ranges from 0.2 to 1.0 just before rupture. The upper surface remains flat during almost the whole process. Just at the end it shows a tiny variation between 0.993 and 1.04.

VI. CONCLUSION

We have studied the problem of two thin immiscible liquid layers with a deformable interface and a deformable free surface. An integrated layer model is derived from the Navier-Stokes equations in the long-wave approximation that includes the inertial terms in both layers. This model is analyzed further considering its linear stability with respect to normal harmonic oscillations of the solid substrate. The results are compared with those of the full linearized Navier-Stokes equations discussed in Ref. [21] and with those of the long-wave approximation, given in Appendix B. In this way we found a good agreement at least for the first tongues of the stability diagrams, where the long-wave approximation is valid. Another restriction is given by the size of the acoustic boundary layer $\sqrt{2\nu_i/\tilde{\omega}}$ which should be much smaller in both layers than the critical wavelength. Then the horizontal velocity is always larger than the vertical.

We have examined three different liquid combinations. The first system (A) corresponds to a low viscosity isopropanol film placed on top of a much more viscous oil film. This combination of liquids was used in the recent experiments [22–24] to study mutual adaptation in floating droplets with flexible boundaries. The second system (B) corresponds to a silicone oil on top of a less viscous and heavier water film. When the silicone oil and the water film are interchanged, the system (C) is Rayleigh-Taylor unstable. For all three systems we examine the linear stability of a flat two-layer film under external vibration. Subsequently, the nonlinear temporal evolution of the unstable systems is studied using the integrated model in two and three spatial dimensions for different depth ratios and excitation amplitudes.

If the fluid of the lower layer is heavier, pattern formation is dominated by oscillating squares or hexagons, depending on the layers depth ratio. In case of the square patterns, we find that the elevation regions (droplets) at the upper film surface are located almost perfectly on top of the droplets at the interface. However, each droplet at the interface has a depletion region in its center, thus, resembling a ring shape. The rings appear to be more pronounced for the hexagonal patterns. We remark that regular squares and hexagons have been found experimentally in one-layer films subjected to a vertical vibration with one or two frequencies [8,36].

Interestingly, for some isolated values of the depth ratio and the excitation amplitude, we find larger scale localized structures that form after a quite long evolution time of some thousand oscillation cycles. These localized structures resemble depletion regions (holes), randomly distributed over the interface and over the upper film surface. In fact, the holes can be seen as large-scale defects in the

underlying hexagonal lattice. Previously, highly localized structures have been found experimentally in vibrated one-layer films of high dissipative fluids [40]. These localized structures were found to propagate on top of the immobile regular stripes. On the contrary, the large-scale holes found here remain immobile.

Next, we find a parameter region, where a kind of eightfold quasiperiodic structure occurs. For this parameter, the system seems to be multistable and the outcoming patterns depend on the initial conditions but also on the aspect ratio of the layers. Earlier, similar patterns with eightfold symmetry have been found theoretically in one-layer films in the case of weak viscous dissipation [37,38].

Finally, we study the Rayleigh-Taylor unstable system [configuration (C)] that shows film rupture if the excitation amplitude is zero or small. In the usual case without external vibrations, the upper layer ruptures first, i.e., the interface touches the free surface. If, on the other hand, vibrations are turned on and the amplitude is increased rupture is more and more delayed. For our fluid parameters and the special value of $a = 2.1$ we did not observe rupture within the computed time interval. If the amplitude is further increased, rupture occurs again after rather short times, but now the interface reaches the substrate and the lower layer ruptures first. These findings clearly show the existence of two different regimes, a Rayleigh-Taylor regime (small a), when the Rayleigh-Taylor instability dominates the dynamics and a Faraday regime (large a), when the nonlinear evolution is dictated by the vibrations. For intermediate values of the amplitude, the layers are stabilized. A stabilizing effect of the vibration has been previously reported for dewetting one-layer liquid films [41]. In the absence of vibration, a dewetting flat film ruptures due to the destabilizing action of the intermolecular forces. However, when vibrated, the rupture was shown to be delayed or completely suppressed, similar to the findings reported here for the Rayleigh-Taylor unstable two-layer films. This points towards a universal nature of the vibration as a stabilization tool in hydrodynamic systems with deformable interfaces. Indeed, the external vibration has been shown to act stabilizing, both in the linear regimes (stabilization for the Rayleigh-Taylor instability in flat films [31,32]), as well as in the nonlinear regimes, as a tool for film rupture suppression.

ACKNOWLEDGMENTS

This work was supported by the Swinburne University of Technology under the Visiting Researcher Scheme. M.B. thanks the Department of Mathematics for kind hospitality during a research stay in Melbourne.

APPENDIX A: MATRIX ELEMENTS

The matrix $\underline{M}$ from (31) reads

$$\underline{M}(h_i) = \frac{1}{D(h_i)} \begin{pmatrix} -h_2^2\left(\frac{\mu h_2}{3} + h_1\right) & \frac{h_1^2 h_2}{2} \\ h_1^2 h_2 & -\frac{2h_1^3}{3} \end{pmatrix} \tag{A1}$$

with

$$D(h_i) = \tfrac{2}{9}\,\mu h_1^3 h_2^3 + \tfrac{1}{6}\,h_1^4 h_2^2 \tag{A2}$$

as the determinant of the inverse of $\underline{\mathrm{M}}$.

The matrix $\underline{A}$ from(40) reads

$$\underline{A}(h_i) = \begin{pmatrix} \frac{-2h_1h_2^2}{D(h_i)}\left(\frac{\mu h_2}{3} + h_1\right) & \frac{h_1^3 h_2}{D(h_i)} & h_1[(\Gamma_1 + \Gamma_2)k^3 + Gk] & h_1[\Gamma_2 k^3 + Gk/\rho] \\ \frac{\rho h_1^2 h_2^2}{D(h_i)} & -\frac{2\rho h_1^3 h_2}{3D(h_i)} & h_2[\rho\Gamma_2 k^3 + Gk] & h_2[\rho\Gamma_2 k^3 + Gk] \\ -k & 0 & 0 & 0 \\ 0 & -k & 0 & 0 \end{pmatrix}; \tag{A3}$$

the nonzero elements of $\underline{B}$ are given as

$$\begin{aligned} B_{13}(h_i,t) &= Gh_1 ka\cos\omega t,\\ B_{14}(h_i,t) &= B_{13}(h_i,t)/\rho,\\ B_{23}(h_i,t) &= B_{24}(h_i,t) = Gh_2 ka\cos\omega t. \end{aligned} \tag{A4}$$

The two matrices $\underline{Q}_i$ from (51) are found from the dyadic products

$$\underline{Q}_1 = \int_0^{h_1} dz\, \vec{u}_1 \otimes \vec{u}_1, \quad \underline{Q}_2 = \int_{h_1}^{h_1+h_2} dz\, \vec{u}_2 \otimes \vec{u}_2. \tag{A5}$$

The elements of $\underline{Q}_i$ are given as

$$\begin{aligned} Q_1^{ij} &= \frac{h_1^3}{3}\left(\frac{8}{5}h_1^2\Phi_1^i\Phi_1^j + h_2^2\Phi_2^i\Phi_2^j\right) + \frac{5}{12}h_1^4h_2\left(\Phi_1^i\Phi_2^j + \Phi_2^i\Phi_1^j\right),\\ Q_2^{ij} &= h_1^4h_2\Phi_1^i\Phi_1^j + \frac{2}{3}h_2^3\Phi_2^i\Phi_2^j\left(\frac{1}{5}\mu^2h_2^2 + \mu h_1h_2 + \frac{3}{2}h_1^2\right) + h_1^2h_2^2\left(h_1 + \frac{1}{3}\mu h_2\right)\left(\Phi_1^i\Phi_2^j + \Phi_2^i\Phi_1^j\right), \end{aligned} \tag{A6}$$

with $i,j = x,y$.

APPENDIX B: LINEAR STABILITY OF A FLAT TWO-LAYER FILM WITH RESPECT TO LONG-WAVE PERTURBATIONS

We study the linear stability of a motionless steady state of Eqs. (9), (13), (20), and (21) that corresponds to a flat two-layer film with $h_1 = h_1^0$, $h_2 = h_2^0$, and $u_i = w_i = 0$.

At the onset of the Faraday instability we may apply Floquet's theorem and expand

$$\begin{aligned} u_j(x,t) &= -\frac{i}{k}\sum_{n=-\infty}^{\infty} e^{i\omega nt/2}\int dk\, u_n^{(j)}(k)e^{-ikx},\\ h_j(x,t) &= h_i^0 + \sum_{n=-\infty}^{\infty} e^{i\omega nt/2}\int dk\, h_n^{(j)}(k)e^{-ikx}. \end{aligned} \tag{B1}$$

Using (B1) we linearize Eqs. (9), (13), (20), and (21) about the trivial steady state and obtain in Fourier space

$$\begin{aligned} \frac{i\omega n}{2}u_n^{(1)} &= \partial_{zz}^2u_n^{(1)} - f_n^{(1)}, \quad \frac{i\omega n}{2}u_n^{(2)} = \frac{\rho}{\mu}\partial_{zz}^2u_n^{(2)} - f_n^{(2)},\\ \frac{i\omega n}{2}h_n^{(1)} &= \int_0^{h_1^0} u_n^{(1)}\,dz, \quad \frac{i\omega n}{2}h_n^{(2)} = \int_{h_1^0}^{h_1^0+h_2^0} u_n^{(2)}\,dz, \end{aligned} \tag{B2}$$

where

$$\begin{aligned} f_n^{(1)} &= h_n^{(1)}(Gk^2 + (\Gamma_1+\Gamma_2)k^4) + h_n^{(2)}\left(G\frac{k^2}{\rho} + \Gamma_2k^4\right)\\ &\quad + \frac{aGk^2}{2}\left(h_{n+2}^{(1)} + h_{n-2}^{(1)}\right) + \frac{aGk^2}{2\rho}\left(h_{n+2}^{(2)} + h_{n-2}^{(2)}\right),\\ f_n^{(2)} &= \left(h_n^{(1)} + h_n^{(2)}\right)(Gk^2 + \rho\Gamma_2k^4) + \frac{aGk^2}{2}\left(h_{n+2}^{(2)} + h_{n-2}^{(2)} + h_{n+2}^{(1)} + h_{n-2}^{(1)}\right). \end{aligned} \tag{B3}$$

For $n \neq 0$, the solution of the first two equations in Eq. (B2) is

$$u_n^{(1)} = A_n^{(1)} e^{zq_1} + A_n^{(2)} e^{-zq_1} - \frac{2 f_n^{(1)}}{i\omega n},$$
$$u_n^{(2)} = B_n^{(1)} e^{zq_2} + B_n^{(2)} e^{-zq_2} - \frac{2 f_n^{(2)}}{i\omega n}, \tag{B4}$$

with $q_1^2 = i\omega n/2$ and $q_2^2 = i\mu\omega n/(2\rho)$. For $n = 0$ the only possible solution is $u_0^{(i)} = 0$, implying $f_0^{(i)} = 0$.

The coefficients $A_n^{(i)}$ and $B_n^{(i)}$ can be expressed as linear combinations of $f_n^{(i)}$ by using the four boundary conditions (8), (10), (11), and (14). After substituting (B4) into the last two equations in (B2) and solving the integrals over z, we obtain a closed linear system of equations for the expansion coefficients $h_n^{(i)}$,

$$-\left\{ \frac{\omega^2 n^2}{2k^2} \begin{pmatrix} M_n^{(11)} & M_n^{(12)} \\ M_n^{(21)} & M_n^{(22)} \end{pmatrix}^{-1} + \begin{pmatrix} G + (\Gamma_1 + \Gamma_2)k^2 & G\rho^{-1} + \Gamma_2 k^2 \\ G + \rho\Gamma_2 k^2 & G + \rho\Gamma_2 k^2 \end{pmatrix} \right\} \begin{pmatrix} h_n^{(1)} \\ h_n^{(2)} \end{pmatrix}$$
$$= \frac{aG}{2} \begin{pmatrix} h_{n+2}^{(1)} + h_{n-2}^{(1)} + \left(h_{n+2}^{(2)} + h_{n-2}^{(2)}\right)\rho \\ h_{n+2}^{(1)} + h_{n-2}^{(1)} + h_{n+2}^{(2)} + h_{n-2}^{(2)} \end{pmatrix}, \tag{B5}$$

where the elements of the matrix $M_n^{(jk)}$ are given by

$$M_n^{(11)} = C q_1^{-1}\left(e^{q_1 h_1^0} + e^{-q_1 h_1^0} - 2\right) - 2q_1^{-1}\left(e^{-q_1 h_1^0} - 1\right) - 2h_1^0,$$
$$M_n^{(12)} = F q_1^{-1}\left(e^{q_1 h_1^0} + e^{-q_1 h_1^0} - 2\right),$$
$$M_n^{(21)} = D q_2^{-1}\left(e^{2q_2 - q_2 h_1^0} - e^{q_2 h_1^0}\right),$$
$$M_n^{(22)} = S q_2^{-1}\left(e^{2q_2 - q_2 h_1^0} - e^{q_2 h_1^0}\right) - 2\left(1 - h_1^0\right), \tag{B6}$$

with

$$C = \frac{2\left(1 - e^{-q_1 h_1^0}\right)\left(e^{q_2 h_1^0 - 2q_2} - e^{-q_2 h_1^0}\right) - 2\sqrt{\rho\mu}\, e^{-q_1 h_1^0}\left(e^{q_2 h_1^0 - 2q_2} + e^{-q_2 h_1^0}\right)}{\left(e^{q_1 h_1^0} - e^{-q_1 h_1^0}\right)\left(e^{q_2 h_1^0 - 2q_2} - e^{-q_2 h_1^0}\right) - \sqrt{\rho\mu}\left(e^{q_2 h_1^0 - 2q_2} + e^{-q_2 h_1^0}\right)\left(e^{q_1 h_1^0} + e^{-q_1 h_1^0}\right)},$$
$$F = \frac{-2\left(e^{q_2 h_1^0 - 2q_2} - e^{-q_2 h_1^0}\right)}{\left(e^{q_1 h_1^0} - e^{-q_1 h_1^0}\right)\left(e^{q_2 h_1^0 - 2q_2} - e^{-q_2 h_1^0}\right) - \sqrt{\rho\mu}\left(e^{q_2 h_1^0 - 2q_2} + e^{-q_2 h_1^0}\right)\left(e^{q_1 h_1^0} + e^{-q_1 h_1^0}\right)},$$
$$D = \sqrt{\rho\mu}\frac{C\left(e^{q_1 h_1^0} + e^{-q_1 h_1^0}\right) - 2e^{-q_1 h_1^0}}{e^{q_2 h_1^0} - e^{-q_2 h_1^0} e^{2q_2}},$$
$$S = \sqrt{\rho\mu}\frac{F\left(e^{q_1 h_1^0} + e^{-q_1 h_1^0}\right)}{e^{q_2 h_1^0} - e^{-q_2 h_1^0} e^{2q_2}}. \tag{B7}$$

Note that (B5) holds also for $n = 0$ where the matrix $\underline{M}$ is not needed. To evaluate (B5) numerically, we truncate the expansions (B1) after a certain number of modes N and take $-N \leqslant n \leqslant N$. In order to control the accuracy of the numerical solution, we vary the number of modes between $N = 25$ and $N = 50$. Then (B5) can be written as a generalized $(4N + 2)$-dimensional eigenvalue problem with $aG/2$ representing its eigenvalues. It is solved by the LAPACK routine GGEV for a given combination of the fluid parameters and the wave vector k. In this way we find the critical amplitudes $a(k)$ for the onset of the Faraday instability which are plotted in Figs. 2–5.

[1] M. Faraday, On a peculiar class of acoustical figures, Philos. Trans. R. Soc. London **121**, 299 (1831).
[2] S. Douady, Experimental study of the Faraday instability, J. Fluid Mech. **221**, 383 (1990).
[3] T. B. Benjamin and F. Ursell, The stability of the plane free surface of a liquid in vertical periodic motion, Proc. R. Soc. London, Ser. A **225**, 505 (1954).
[4] K. Kumar and L. S. Tuckerman, Parametric instability of the interface between two fluids, J. Fluid Mech. **279**, 49 (1994).
[5] J. Beyer and R. Friedrich, Faraday instability: Linear analysis for viscous fluids, Phys. Rev. E **51**, 1162 (1995).
[6] J. Bechhoefer, V. Ego, S. Manneville, and B. Johnson, An experimental study of the onset of parametrically pumped surface waves in viscous fluids, J. Fluid Mech. **288**, 325 (1995).
[7] C. Wagner, H.-W. Müller, and K. Knorr, Pattern formation at the bicritical point of the Faraday instability, Phys. Rev. E **68**, 066204 (2003).
[8] W. S. Edwards and S. Fauve, Patterns and quasi-patterns in the Faraday experiment, J. Fluid Mech. **278**, 123 (1994).
[9] B. Christiansen, P. Alstrom, and M. T. Levinsen, Ordered Capillary-Wave States: Quasicrystals, Hexagons and Radial Waves, Phys. Rev. Lett. **68**, 2157 (1992).
[10] W. S. Edwards and S. Fauve, Parametrically excited quasicrystalline surface waves, Phys. Rev. E **47**, R788 (1993).
[11] Y. Ding and P. Umbanhowar, Enhanced Faraday pattern stability with three-frequency driving, Phys. Rev. E **73**, 046305 (2006).
[12] P. Chen and K.-A. Wu, Subcritical Bifurcations and Nonlinear Balloons in Faraday Waves, Phys. Rev. Lett. **85**, 3813 (2000).
[13] P. Chen, Nonlinear wave dynamics in Faraday instabilities, Phys. Rev. E **65**, 036308 (2002).
[14] S. Ubal, M. D. Giavedoni, and F. A. Saita, A numerical analysis of the influence of the liquid depth on two-dimensional Faraday waves, Phys. Fluids **15**, 3099 (2003).
[15] N. Perinet, D. Juric, and L. S. Tuckerman, Numerical simulation of Faraday waves, J. Fluid Mech. **635**, 1 (2009).
[16] N. Perinet, D. Juric, and L. S. Tuckerman, Alternating Hexagonal and Striped Patterns in Faraday Waves, Phys. Rev. Lett. **109**, 164501 (2012).
[17] L. Kahouadji, N. Perinet, L. S. Tuckerman, S. Shin, J. Chergui, and D. Juric, Numerical simulation of supersquare patterns in Faraday waves, J. Fluid Mech. **772**, R2 (2015).
[18] M. Bestehorn, Q. Han, and A. Oron, Nonlinear pattern formation in thin liquid films under external vibrations, Phys. Rev. E **88**, 023025 (2013).
[19] M. Bestehorn, Laterally extended thin liquid films with inertia under external vibrations, Phys. Fluids **25**, 114106 (2013).
[20] R. V. Craster and O. K. Matar, Dynamics and stability of thin liquid films, Rev. Mod. Phys. **81**, 1131 (2009).
[21] A. Pototsky and M. Bestehorn, Faraday instability of a two-layer liquid films with a free upper surface, Phys. Rev. Fluids **1**, 023901 (2016).
[22] G. Pucci, E. Fort, M. Ben Amar, and Y. Couder, Mutual Adaptation of a Faraday Instability Pattern with its Flexible Boundaries in Floating Fluid Drops, Phys. Rev. Lett. **106**, 024503 (2011).
[23] G. Pucci, M. Ben Amar, and Y. Couder, Faraday instability in floating liquid lenses: The spontaneous mutual adaptation due to radiation pressure, J. Fluid Mech. **725**, 402 (2013).
[24] G. Pucci, M. Ben Amar, and Y. Couder, Faraday instability in floating drops, Phys. Fluids **27**, 091107 (2015).
[25] A. Oron, S. H. Davis, and S. G. Bankoff, Long-scale evolution of thin liquid films, Rev. Mod. Phys. **69**, 931 (1997).
[26] K. Kumar, Linear theory of Faraday instability in viscous liquids, Proc. R. Soc. London, Ser. A **452**, 1113 (1996).
[27] A. Pototsky, M. Bestehorn, D. Merkt, and U. Thiele, Morphology changes in the evolution of liquid two-layer films, J. Chem. Phys. **122**, 224711 (2005).
[28] S. Chandrasekhar, *Hydrodynamic and Hydromagnetic Stability* (Dover, New York, 1981).

[29] E. Anderson, Z. Bai, J. Dongarra, A. Greenbaum, A. McKenney, J. Du Croz, S. Hammerling, J. Demmel, C. Bischof, and D. Sorensen Lapack, A portable linear algebra library for high-performance computers, in *Proceedings of the 1990 ACM/IEEE Conference on Supercomputing, Supercomputing '90, New York* (IEEE Computer Society Press, Los Alamitos, CA, 1990), p. 2.

[30] W. H. Press, B. P. Flannery, S. A. Teukolsky, and W. T. Vetterling, *Numerical Recipes*, 3rd ed. (Cambridge University Press, New York, 2007).

[31] F. M. Hoffmann and G. H. Wolf, Excitation of parametric instabilities in statically stable and unstable fluid interfaces, J. Appl. Phys. **45**, 3859 (1974).

[32] F. Troyon and R. Gruber, Theory of the dynamic stabilization of the Rayleigh-Taylor instability, Phys. Fluids **14**, 2069 (1971).

[33] V. Lapuerta, F. J. Mancebo, and J. M. Vega, Control of Rayleigh-Taylor instability by vertical vibration in large aspect ratio containers, Phys. Rev. E **64**, 016318 (2001).

[34] M. Silber, C. Topaz, and A. C. Skeldon, Two-frequency forced Faraday waves: Weakly damped modes and pattern selection, Phys. D (Amsterdam, Neth.) **143**, 205 (2000).

[35] A. C. Skeldon and G. Guidoboni, Pattern Selection for Faraday Waves in an Incompressible Viscous Fluid, SIAM J. Appl. Math. **67**, 1064 (2007).

[36] D. Binks and W. van de Water, Nonlinear Pattern Formation of Faraday Waves, Phys. Rev. Lett. **78**, 4043 (1997).

[37] W. Zhang and J. Viñals, Square patterns and quasipatterns in weakly damped Faraday waves, Phys. Rev. E **53**, R4283 (1996).

[38] W. Zhang and J. Viñals, Pattern formation in weakly damped parametric surface waves, J. Fluid Mech. **336**, 301 (1997).

[39] H. Arbell and J. Fineberg, Temporally Harmonic Oscillons in Newtonian Fluids, Phys. Rev. Lett. **85**, 756 (2000).

[40] C. Cabeza, C. Negreira, and V. Gibiat, Coexistence of localized structures and patterns in Farady instability for high dissipative fluids, Int. J. Bifurcation Chaos **14**, 3355 (2004).

[41] S. Shklyaev, M. Khenner, and A. A. Alabuzhev, Enhanced stability of a dewetting thin liquid film in a single-frequency vibration field, Phys. Rev. E **77**, 036320 (2008)